

Original Article

e-ISSN: 2581-0545 - <https://journal.itera.ac.id/index.php/jsat/>

Active contour driven by scalable local regional information on expandable kernel

Received 13th March 2020
Accepted 12th June 2020
Published 15th June 2020

Open Access

DOI: 10.35472/jsat.v4i1.262

Amir Faisal *^a, Charnchai Pluemtiwiriawej ^b^a Department of Biomedical Engineering, Institut Teknologi Sumatera, Lampung Selatan, Indonesia, 35365^b Department of Electrical Engineering, Chulalongkorn University, Bangkok, Thailand, 10330* Corresponding E-mail: amir.faisal@bm.itera.ac.id

Abstract: An active contour that uses the pixel's intensity on a set of expandable kernels along the propagating contour is presented in this paper. The objective in this study is to employ the scalable kernels to drive the contour to meet the intended boundary. The key characteristics of this scheme is that the kernels gradually expand to find an object's boundary. So this scheme could penetrate to the concave boundary more effective and efficient than some other schemes. If a Gaussian kernel is applied, it could trace the object with a blurred or smooth boundary. Moreover, the directional selectivity feature enables in capturing two edge's types with just one initial position. Its performance showed more desirable segmentation outcomes compared to the other existing active contours using regional information when segmenting the noisy image and the non-uniform (or heterogeneous) textures. Meanwhile, the level set implementation enables topological flexibility to our active contour scheme.

Keywords: *active contour, directional selectivity, image segmentation, level set, local adaptation process, kernel, scalability*

Introduction

Active contours [1]-[6] had been extensively used in addressing the image segmentation problems. The contour propagates from its initial position until it arrived at the region of interest. An energy function associated with the contour's smoothness and the image characteristics is optimized by a gradient flow to regulate the contour motion, such that when the contour coincides with the boundaries, the function should reach its optimum. Two often used categories of the image features are the object's edge and the regional information. Edge-based models compute the image gradient priori and use the obtained edge pixels as boundary candidates. As a result, the image becomes non-zero at the rapid intensity changes, supposedly the actual boundaries. The spatial intensity variation such as the non-uniform background may disappear while a rapid intensity change was converted into the edges. In fact, not only the boundaries but also the noises attribute as the rapid intensity changes. Since the force on the contour front depends on such image gradient, the contour deforms gradually either inward or outward before finally stopped on the strong edges where the magnitude of the force was minimal. However, it often evolves slowly with a small capture range. The additional balloon force may gain a faster convergence and a larger capture range despite making it sensitive to

initialization. To reduce the sensitivity to the noises, a Gaussian smoothing filter and a balloon force may be tuned with larger value. But, it also results in the blurring the true boundaries making the contour pass through the noises and the weak boundaries or the occluded objects. To overcome these classical drawbacks of the image gradient, the regional information uses statistics of several pixels within an object's region to drive the contour to meet the boundary. There have been several regional descriptors for active contours in the literature. They can be categorized into four categories according to the data fitting terms or the energy measures. They are the global regional information, the scalable global regional information, the scalable local regional information, and the local regional information as illustrated in **Figures 1**.

The organization of this paper is given as follows. Various regional descriptors of existing active contours are reviewed and classified in the next section. Section III describes our presented active contour scheme. In Section IV, the experimental results comparing our scheme with the other existing schemes on real and synthetic images are discussed. The last section concludes the paper.



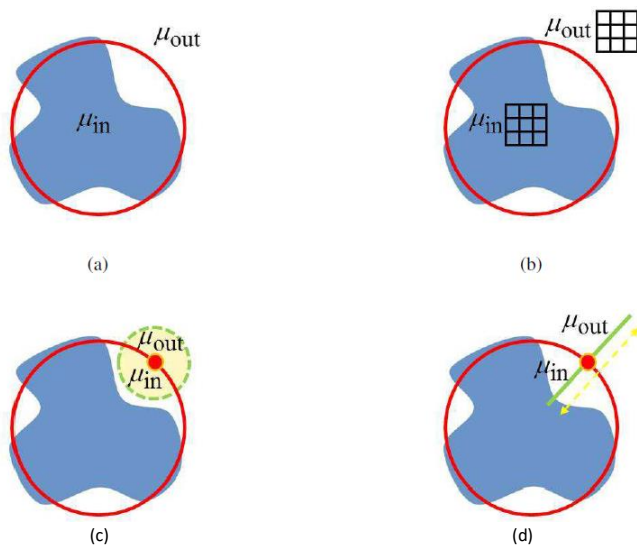


Figure 1. Various regional descriptors of existing active contour schemes using; (a) global regional information, (b) scalable global regional information, (c) scalable local regional information, and (d) local regional information.

Regional Descriptors For Active Contour Schemes

The Global Regional Information Scheme

In 1989, Mumford and Shah [9] introduced theoretical scheme of the piecewise smooth model that provides the foundation to the global regional image segmentation. Later, Tsai et al [10] and Vese and Chan [11] implemented it independently using the level set method [7]. The piecewise smooth model of Mumford-Shah [9] assumed the region to be smooth with a slow variation; whereas, its simplification, the piecewise constant model of Chan and Vese [12] estimated the regions by the the constant intensity averages on the either image regions delimited by the contour. When the means approximated the regions optimally, this energy is minimized. Later, Yezzi et al. [13] included the regional variances to the model's statistics. Michailovich et al. [14] minimized the probability density functions of the intensity histograms on the two sides of the contour. Note that these models used the global regional data fitting functions or statistics in both sides the contour as a clue to detect the boundary. Hence, they were called as the global regional schemes.

The Scalable Global Regional Information Scheme

Li et al. [16] proposed a region-scalable fitting (RSF) scheme to deal with the non-uniform textures, which could not be distinguished using the previous global energy measure, by sliding the fixed-scale Gaussian

kernels into every pixels in the interior and exterior of the contour. The scalable kernel allowed an estimation of the mean intensity at a regional Gaussian sigma from the small to large size. The kernel was of fixed size and did not change during the contour evolution. Thus, it was included as a global scalable regional information. The similar scheme could also be found in [17], [18]. Brox and Cremers [19] interpreted this scheme as the statistical piecewise smooth model where their efficient implementation techniques were presented in [19], [20]. Its relationship with the Bayesian models, its extension, and simplification were derived in [19] as well. These schemes have also been extended to the simultaneous bias correction [40], [39], [41], [38] and multiphase segmentation [21] where its implementation without active contour offered even more efficient performance [22]. [40] tackled this non-uniform intensity problem using spatially locally varying mean and variance but does not take into account the variance component that is included in [38]. Similar to [38], [40] was implemented to jointly approximate the multiplicative bias component while segmenting the images.

The use of the kernel suffered the disadvantages of using the local energy measures. The small size kernel provided the local intensity estimation but the least difference in statistics, which led to (almost) no contour evolution on a homogeneous area. While large size kernel estimated intensity similar to the global regional energy measure. Piovano and Papadopoulou [23] modified [20] to tackle the local minima problem which also caused the global coherence problem by finding the minimum size larger than a threshold to generate an evolution and adding the directional scheduling regarding the local inner and outer statistics. In addition, [43], [42] were introduced in order to stabilize the level set function.

Utilizing the entire image feature on the either regions of the contour, these two global regional statistics behaved as a gravitational field to segment the image into some areas represented by the contour. The global regional schemes allowed an intensity approximation of the whole image and had no selection to estimate a smaller area. The scalable global regional schemes, on contrary, provided the selection of the size from the local neighbourhood to the whole image.

The Scalable Local Regional Information Scheme

The global data fitting method may produce a poor segmentation result due to the overlapped probability

densities of the inhomogenous textures between the foreground and the background. Reducing the overlapping distributions analogously to the local edge assumption, Lankton and Tannenbaum [24] and Darolti et al. [25] introduced active contours using local statistics to sample the image intensity inside a set of the predetermined-size balls (LRAC) and square windows (LRD) along the contour pixels. The local regions were formed by dividing the window with the contour front while the rest of image features were not included. These models were considered as the local scalable regional active contours.

The inability to measure the intensity statistics outside the fixed-scale window on the homogeneous region contributed to the zero statistics force. The user needed to set a kernel size priori and appropriately. If the initial contour was positioned far from the object and the kernel size is too small, the contour could not find any concave boundaries. Consequently, it had a diminished capture range because the small kernels may not have enough samples to induce the motion. On the other hand, the large scale tend to ignore the intensity details which may lead to the segmentation inaccuracy, a global regional method behaviour. It is hard to set a proper scale when different concave boundaries existed. As long as the window found the boundary with enough information, the contour position on the boundary is the least affected and accurate in general. To tackle the contour not to stuck in the local minima during finding the boundary, the LRD utilized the balloon force to grow the contour. The local statistics near the boundary was then different enough to stop the contour. The balloon force limits the initial position to be placed only inside object's boundary. It was still not clear that the LRD was able in capturing any concave boundaries.

While the aforementioned models [24]-[25] had a slightly similar idea in embedding the scalable window on the contour points, the authors [29]-[31] embedded a local energy measure along the neighbourhood band on both sides of the contour with an adjustable width. Dealing with the heterogeneous textures, J. Mille [29] introduced an active contour using narrowband region where two intensity variances were calculated within the fixed-thickness regions both sides the contour. The small width contributed to the local minima problems while the large width led to the global constraint properties. Consequently, it had a poor capture range when the energy measures had the least difference statistics. Li and Yezzi [30] presented the dual-front

active contours. The dilation and erosion operations were employed to lengthen the narrow active region both side the contour with an adjustable width using a certain criteria. Ronfard [31] employed an adaptive-width region, using the separate and non-overlapping neighbourhood, around the parametric contour. Although this model did not explicitly address the non-uniform and heterogeneous textures problems, this framework allowed adapting the neighbourhood width and merging to form a larger band when the homogeneous area did not give the statistics force.

The Local Regional Information Scheme

Using the parametric contour, Karaolani et al. [26] presented an active contour using finite elements to regulate the local neighborhood. A local regional force was generated from a certain number of the sampled local intensity elements along the contour, hence, the segmentation accuracy depended on the number of elements. Inspired by [28], [12], Phumeechanya et al. [27] presented an active contour using local region-based force with extendable search lines (LRES). While [28] used the normal lines of pre-determined fixed-length to detect the image edges, the LRES drives the contour using the local information on the normal extendable lines to reach the concave boundary. It had a superiority in handling the heterogeneous texture images. Nevertheless, different with the scalable RSF's Gaussian kernel and LRAC's ball mask, the LRES forces were determined from the search lines whose the area was thin and not proportional, hence, not scalable to a large image area. Despite the search line was extendable, its area did not change much, thus, was unable to mask either significantly smaller or larger image areas. These models were therefore categorized as the local regional schemes. Moreover, the unscalable search lines may provided insufficient statistics, thus, produced a relatively low force. Consequently, the LRES algorithm was time consuming.

These two local regional models tried to locate the boundaries by gradually deforming the contour similar to those in the edge information schemes. The local regional schemes only estimated the local intensity but did not accommodate any scale choice to measure the region with various sizes. Meanwhile, the local scalable regional schemes had a flexibility to estimate the intensity statistics using various scales of the kernel.

In this paper, an active contour method employing scalable local regional (SLR) statistics on expandable kernel is presented. Our active contour uses various size kernels to direct the contour to meet the boundary. The kernels are centered on the evolving contour as shown in **Figure 2**. The kernel is of adaptive scale during the contour's evolution. The kernel size adaptation is regulated by the local pixel's intensity. The kernel is expanded slowly until enough statistics provide the contour the direction to detect an object's boundary. In this manner, the objects with the concave boundary within the image domain could be captured, in contrast to the fixed-scale window that does not induce any evolution if it did not detect any object. The various scale that adaptively changes help the method to capture the concave boundary with a large range. Meanwhile, the scalable local regional information enables segmentation of images with non-uniform and heterogeneous textures at a rapid convergence rate. Our model with Gaussian kernel could trace both smooth or blurred boundary. The level set formulation accommodated our contour a topological flexibility. In addition, The directional selectivity property was extracted from our model to attract the two objects with different edge's types using one initial contour. Both schemes have been presented in [32], [37] where its extension for multiple region segmentation has been presented in [44], [45].

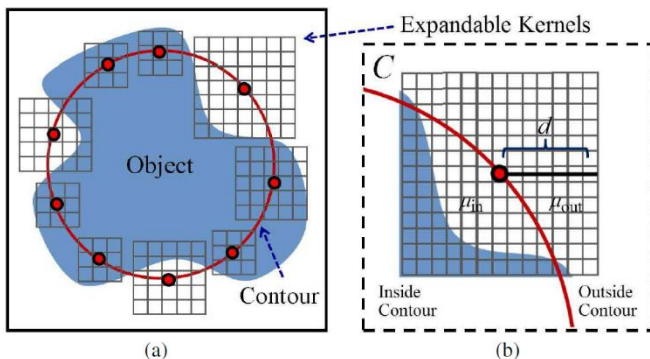


Figure 2. Scalable local region on expandable kernel [32]

Method

The Scalable Local Regional (SLR) Information

Our active contour is implemented via the level set method. One of its advantages is that any topological changes during

its evolution is handled by itself. Let Ω be the image spatial domain and the evolving contour at time t , $C(t) \subset \Omega$ be embedded as the zero level of the level set function $\phi(\mathbf{x}) \rightarrow \mathfrak{R}$, where \mathfrak{R} is a set of real numbers.

$$C(t) = \{\mathbf{x} \in \Omega : \phi(\mathbf{x}, t) = 0\} \text{ with } \phi(\mathbf{x}, 0) = C_0, \quad (1)$$

where C_0 is initial contour. Define the smooth Heaviside function $H_\epsilon(\phi)$ and the smooth Dirac delta function $\delta_\epsilon(\phi)$ as in (2) and (3), respectively [12]. The inner region, outer region, and the region around the contour are represented by $H_\epsilon(\phi)$, $1 - H_\epsilon(\phi)$, and $\delta_\epsilon(\phi)$, respectively.

$$H_\epsilon(\phi) = \begin{cases} 1 & \text{if } \phi > \epsilon \\ 0 & \text{if } \phi < -\epsilon, \\ \frac{1}{2} \left(1 + \frac{2}{\pi} \arctan \left(\frac{\phi}{\epsilon} \right) \right) & \text{if } |\phi| \leq \epsilon \end{cases} \quad (2)$$

$$\delta_\epsilon(\phi) = \begin{cases} 1 & \text{if } \phi = \epsilon \\ 0 & \text{if } |\phi| < \epsilon, \\ \frac{1}{\pi} \left(\frac{\epsilon}{\pi^2 + \phi^2} \right) & \text{if } |\phi| \leq \epsilon \end{cases} \quad (3)$$

The local regional information used in our SLR scheme is the mean intensity inside the expandable kernels whose the centers are on the contour. The motion of the evolving contour is regulated by such local statistics. The evolving contour separates the kernels centered on the contour into two local regions as in Fig. 2 (b). These regions are formed to measure the scalable local regional statistics, μ_{in} and μ_{out} .

Here the scalable local regional force was derived. A kernel is located along the evolving contour to mask the local region. Let $d = \|\mathbf{x} - \mathbf{y}\|$ be the L_2 norm distance between the kernel's center pixel \mathbf{x} and the other pixels \mathbf{y} within the kernel support. The uniform kernel $K_u(d) = c$, for a positive constant c or a Gaussian kernel $K_G(d) = \frac{1}{(2\pi)^{n/2}\sigma^n} \exp\left(-\frac{d^2}{2\sigma^2}\right)$ can be used. The scalable local regional (SLR) energy in each kernel mask $K(d)$ is defined by

$$E_{SLR}(\phi) = \int_{\Omega} K(\|\mathbf{x} - \mathbf{y}\|) \cdot F(I(\mathbf{x}), \phi(\mathbf{x})) d\mathbf{x}, \quad (4)$$

where I denote the pixels' intensity from an input image. F denote the SLR's energy measure. From three global regional active contour models [12]-[14], two candidates for F are mentioned here.

The Chan-Vese energy function [12], as in (5), assumes the object and background to be of statistically homogeneous. The energy is minimized by their averages intensity values that are approximately at a constant level.

$$F_{CV} = |I(\mathbf{x}) - \mu_{in}(\mathbf{y})|^2 H_\epsilon(\phi(\mathbf{x})) + |I(\mathbf{x}) - \mu_{out}(\mathbf{y})|^2 (1 - H_\epsilon(\phi(\mathbf{x}))). \quad (5)$$

The energy function (6) proposed by Yezzi et al. [13], has an assumption that the intensity average of the foreground and background are very different.

$$F_{MS} = -\frac{1}{2} |\mu_{in}(\mathbf{y}) - \mu_{out}(\mathbf{y})|^2, \quad (6)$$

where μ_{in} and μ_{out} represent the local mean intensities of both regions inside the kernel $K(\mathbf{x} - \mathbf{y})$ separated by the contour, given by

$$\mu_{in}(\mathbf{y}) = \frac{\int_{\Omega} K(\|\mathbf{x} - \mathbf{y}\|) H_\epsilon(\phi(\mathbf{x})) I(\mathbf{x}) d\mathbf{x}}{\int_{\Omega} K(\|\mathbf{x} - \mathbf{y}\|) H_\epsilon(\phi(\mathbf{x})) d\mathbf{x}}, \quad (7)$$

$$\mu_{out}(\mathbf{y}) = \frac{\int_{\Omega} K(\|\mathbf{x} - \mathbf{y}\|) (1 - H_\epsilon(\phi(\mathbf{x}))) I(\mathbf{x}) d\mathbf{x}}{\int_{\Omega} K(\|\mathbf{x} - \mathbf{y}\|) (1 - H_\epsilon(\phi(\mathbf{x}))) d\mathbf{x}}. \quad (8)$$

By taking the derivative of (3) with respect to ϕ , the SLR force is given by

$$F_{SLR} = \int_{\Omega} K(\|\mathbf{x} - \mathbf{y}\|) \frac{\partial F(I(\mathbf{x}), \phi(\mathbf{x}))}{\partial \phi(\mathbf{x})} d\mathbf{x}. \quad (9)$$

To fully express F_{SLR} , derivative of the aforementioned energies, F_{CV} and F_{MS} , is taken with respect to ϕ . $\frac{\partial F(I(\mathbf{x}), \phi(\mathbf{x}))}{\partial \phi(\mathbf{x})}$ becomes

$$\frac{\partial F_{CV}}{\partial \phi} = \delta_\epsilon(\phi(\mathbf{x})) (|I(\mathbf{x}) - \mu_{in}(\mathbf{y})|^2 - |I(\mathbf{x}) - \mu_{out}(\mathbf{y})|^2), \quad (10)$$

$$\frac{\partial F_{MS}}{\partial \phi} = \delta_\epsilon(\phi(\mathbf{x})) (\mu_{in}(\mathbf{y}) - \mu_{out}(\mathbf{y})) \left(\frac{I(\mathbf{x}) - \mu_{in}(\mathbf{y})}{A_{in}} + \frac{I(\mathbf{x}) - \mu_{out}(\mathbf{y})}{A_{out}} \right), \quad (11)$$

where A_{in} and A_{out} are the two areas of our SLR kernel that is separated by the evolving contour, as follows:

$$A_{in} = \int_{\Omega} K(\|\mathbf{x} - \mathbf{y}\|) H_\epsilon(\phi(\mathbf{x})) d\mathbf{x}, \quad (12)$$

$$A_{out} = \int_{\Omega} K(\|\mathbf{x} - \mathbf{y}\|) (1 - H_\epsilon(\phi(\mathbf{x}))) d\mathbf{x}. \quad (13)$$

$$E(\phi) = - \left(\int_{\Omega} \delta_\epsilon(\phi(\mathbf{y})) E_{SLR} d\mathbf{y} - v \int_{\Omega} |\nabla H_\epsilon(\phi(\mathbf{y}))| d\mathbf{y} \right), \quad (14)$$

Our total energy term is shown in (14). ESLR is multiplied with the delta function $\delta_\epsilon(\phi(\mathbf{y}))$ to ensure that there is no new

sudden contours development. Our E_{SLR} only considers pixels distribution within the distance d from the kernel central point and ignores intensity distribution beyond the distance d . The smoothing term is put to control the elasticity of the contour by weighting the arc length of the contour with a parameter v as in (9).

$$\frac{\partial \phi}{\partial t} = \delta_\epsilon(\phi(\mathbf{y})) (F_{SLR} + F_{SM}), \quad (15)$$

$$F_{SM} = v \operatorname{div} \left(\frac{\nabla \phi(\mathbf{y})}{|\nabla \phi(\mathbf{y})|} \right), \quad (16)$$

Finally, we obtain the SLR evolution equation in (15) by taking the derivative of the SLR energy function with respect to ϕ and replacing ϕ with $\phi + \xi \psi$, where ψ represents a small change normal to ϕ weighted by a tiny number ξ . The first term, F_{SLR} , is our scalable local regional force as in (9) to drive the the contour. The second term F_{SM} in (15) as shown in (16) enforces smoothness of the contour.

The Adaptive Local Statistics of the Expandable Kernel

Within a homogeneous foreground or background, the fixed-area window may not induce any motion force. Thus, local adaptation process may overcome the classical drawbacks of the local energy measure. Our method utilizes the kernels of various sizes to meet the boundary of an object. The kernel expands using certain criteria to cover both foreground and background. The kernel size parameterized by the distance d is gradually increasing by setting $d_{initial} + \Delta d$ pixels. It is allowed by checking that the kernel has overlapped any homogeneous region or not. In the homogeneous area, i.e., μ_{in} is the same as μ_{out} . With this condition, the kernel size is expanded. In an inhomogeneous region, supposedly when crossing the boundary, μ_{in} will be significantly different from μ_{out} . The absolute difference of μ_{in} and μ_{out} is compared to a threshold value, τ to check the difference between μ_{in} and μ_{out} . For $\tau \subseteq [0, 1]$ and $L = 255$ for an 8-bit grayscale image, the threshold of the uniform kernel is $[L * \tau]$. The threshold of the Gaussian kernel can be chosen between 0 and 1 because the normalization constant satisfies $\int K_G(\|\mathbf{x} - \mathbf{y}\|) d\mathbf{x} = 1$.

The SLR force informs the contour to move inward or outward depending on the magnitude of the difference between intensity profile within the kernel, I , and μ_{in} or μ_{out} . If I is closer to μ_{out} than μ_{in} , a positive sign of the SLR force locally drive the contour inward. On a contrary, if I is the same value as μ_{in} and different from μ_{out} , its negative sign drives the contour in the outward direction. The

magnitude of this force is normalized to have value in a range $[-1,1]$. It is a force to drive the contour for one iteration. Another iteration is started by setting $d_i = d_{\text{initial}}$ then repeat the process of the kernel adaptation. The evolution stops once there is no longer difference between I and μ_{in} or μ_{out} to induce more statistics force. The overall local adaptation process of expandable kernel is illustrated in the flow chart of **Figure 3** [32].

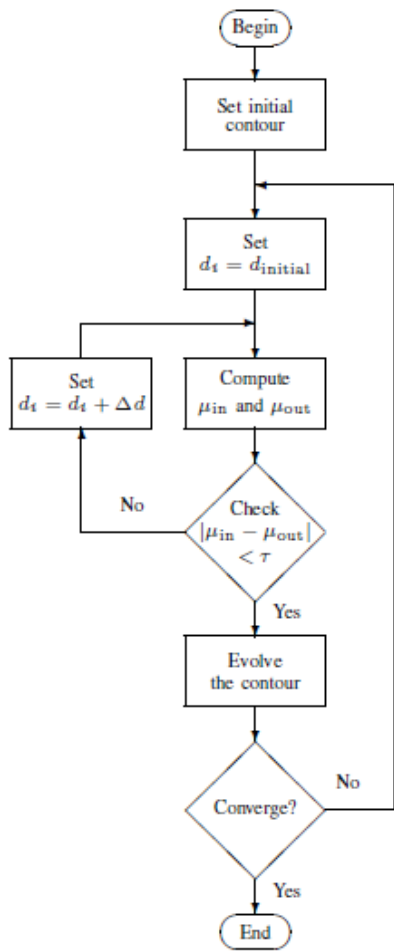


Figure 3. Flow chart of our SLR active contour evolution step [32]

The Directional Scalable Local Regional (DSLR) Feature

Some images may be difficult to be distinguished because they consist of some regions of interest with different kind of the edge and they may overlap or lie on a complex background. Existing models, however, may not direct the contour to certain kind of the edge, thus, could not outline the desired object boundary. With an explicit curve, the directional feature is incorporated to the edge-based models [33]-[35].

Without using image gradient, an edge's type selectable active contour using local regional information with adaptive search line is proposed [36]. Formulated in parametric contour, it employs pixel values along the search lines with adaptive length. The difference of the intensity average on the search line is utilised to choose each object with different edge's type. A balloon force is added to avoid a certain image area. The balloon force limits initial contour to be put in the interior or exterior region of interest only. It also has drawbacks associated with the long thin search line. In addition, those methods with directional feature are using the parametric curve that could not handle topological change [2].

This subsection describes additional feature to our SLR model, i.e., an ability to select object of a particular edge's type, called as the directional scalable local regional using expandable kernel (DSLR) [37]. The pixel's intensity will navigate the contour towards a certain type of object edges using the sign of the difference between μ_{in} and μ_{out} . If μ_{in} is smaller than μ_{out} , it means that the kernel is on a positive edge. On the other hand, μ_{in} will be larger than μ_{out} once it lies on a negative edge. It behaves as a switch [36] to regulate the forces pushing the contour to the desirable edge's type pixels. If the contour points or the kernel crosses an unintended local image area, it needs to be guided away by different force. Therefore, the SLR evolution equation is adjusted as follows.

$$\frac{\partial \phi}{\partial t} = \delta_\epsilon(\phi(y))(F_{\text{SM}} + (1 - \alpha)F_{\text{SLR}} + \alpha F_{\text{LB}}), \quad (17)$$

$$F_{\text{LB}} = \begin{cases} +\omega & \text{inward local balloon} \\ -\omega & \text{outward local balloon} \end{cases} \quad (18)$$

$$\alpha = \text{sign}[\beta \cdot \text{sign}(\mu_{\text{in}} - \mu_{\text{out}}) + 1], \quad (19)$$

$$\text{sign}(z) = \begin{cases} -1 & \text{for } z < 0 \\ 0 & \text{for } z = 0, \\ +1 & \text{for } z > 0 \end{cases} \quad (20)$$

where F_{SM} , F_{SLR} , and F_{LB} are given in (16), (4), and (18), respectively.

As the last term in (17), a local balloon force is added to locally propagate the contour away from an unintended object, where ω is the parameter with positive value that behaves as the speed-size of F_{LB} . F_{LB} is set to $+\omega$ so that the contour will shrink. Using this motion constant, the initialization can be put in the interior or exterior of the object of interest. The switching parameter, α , is put between the F_{SLR} and the F_{LB} . It regulates F_{SLR} and F_{LB} to act alternately according to the image edge. It substitutes the

force by itself for the kernel every iteration. α is either valued 0 or 1. If $\alpha = 0$, F_{SLR} is employed and if $\alpha = 1$, then F_{LB} is employed. The local image may be of positive and negative edges. The positive edge is where a dark foreground lies on a bright background; whereas the negative edge is when a bright foreground is on a dark background. The desirable type of object edge could be selected by setting the parameter β . If the positive edge object is desired to be captured, β value is set to +1 and in the case when the negative-edge object is to be found, β is set to -1. In addition, $\text{sign}(\cdot)$ is the sign function as illustrated in (20). **Figure. 4** illustrates the entire evolution step of our DSLR method.

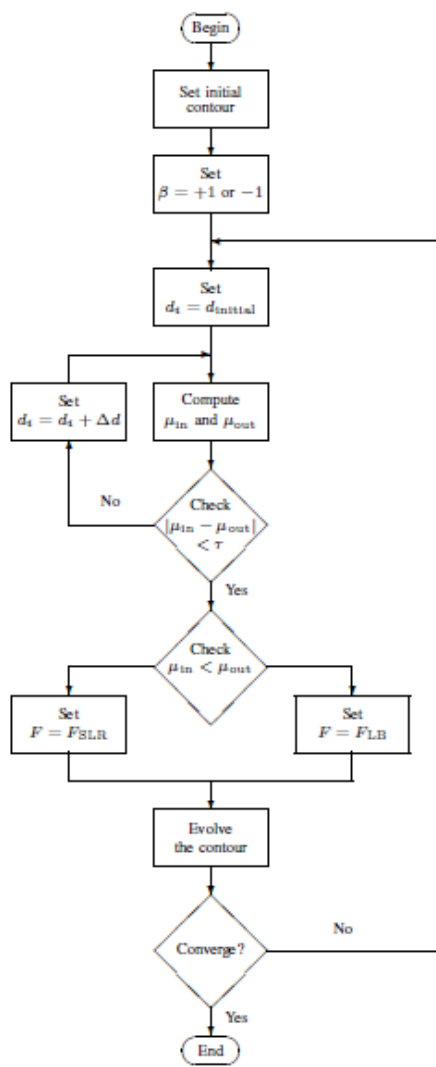


Figure 4. Flow chart of our DSLR evolution step [37].

After the kernel found its optimal size, supposed $\beta = +1$ is set and found that $\mu_{in} < \mu_{out}$, the SLR force navigates the contour. If the kernel crosses a region with $\mu_{in} > \mu_{out}$ then the force is adjusted to the constant motion. For $\beta = -1$, the SLR force direct the contour when $\mu_{in} > \mu_{out}$. The local constant motion is to direct the contour away from fault object boundary when $\mu_{in} < \mu_{out}$. The process is reiterated until the contour meet the boundary.

Results And Discussion

The Scalable Local Regional (SLR) Information

In this section, a number of experiments are conducted using MATLAB to compare our proposed model with other active contour models: ACWE, RSF, LRAC and LRES. In all tests, we set $v = 0.01 \times 255 \times 255$ and $\lambda_1 = \lambda_2 = 1$ for the ACWE, and $v = 0.001 \times 255 \times 255$ and $\lambda_1 = \lambda_2 = 1$ for the RSF, $v = 0.8$ for the LRAC, LRES, and SLR. Each column of **Figures 5** to **7** depicts the initial, the final contours of ACWE, RSF, LRAC, LRES, and our SLR overlaid on the original images, respectively. The computational costs of different methods using local regional information in segmenting different images are compared at **Tables 1** and **2**.

The first row of **Figure 5** shows an air plane image of 200×340 pixels size. All methods generally segment the air plane well. The ACWE and RSF, however, misclassify a small part due to its color is the same with the background. Then, the contours divide and exclude those parts. They converge quickly consuming 10 and 20 iterations with 6.22 and 6.21 seconds. In contrast, the LRAC, LRES, and SLR provide a satisfying boundary. The LRAC needs 1800 iterations with 281.24 seconds while the LRES is more time costly taking 923.61 seconds for 500 iterations. Our SLR's contour stops at 550 iterations with 114.94 seconds.

In the second row of **Figure 5**, segmentation results of a white blood cell image with 200×200 pixels are shown. The U-shape nucleus of the white blood cell is our targeted boundary. The ACWE and RSF not only converge to the nucleus part but also to other parts. The LRES contour is positioned on the entire cell instead of the nucleus itself and needs a costly computing time with 2223.21 seconds for 500 iterations. The LRAC and SLR both obtain satisfying results of only the nucleus and neglecting other areas. Our SLR arrives quicker consuming only 141.58 seconds at 390 iterations.

compared to the LRAC at 433.52 seconds after 1300 iterations.

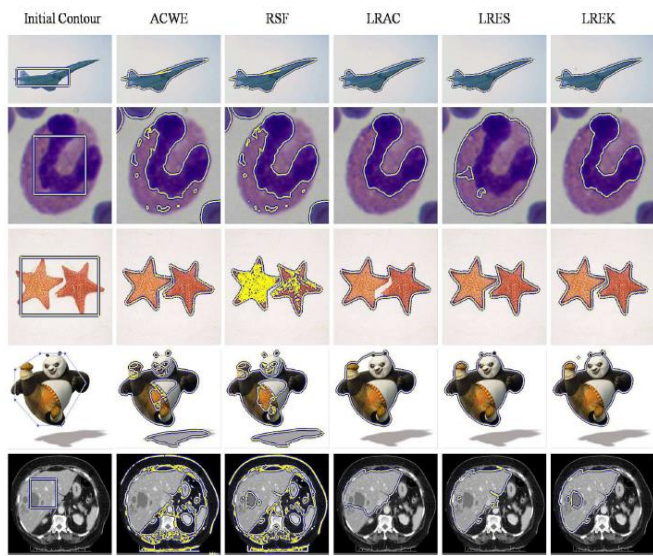


Figure 5. Performance of various active contour scheme; initial and final contour for ACWE, RSF, LRAC, LRES, and SLR, respectively.

Table 1. Computational costs for **Figure 5**.

No.	Image	Method	Number of Iterations	Total Iteration Time (seconds)	Average Time (seconds per iterations)
1	The air plane	LRAC	550	281.24	0.51
		LRES	500	923.61	1.85
		SLR	550	114.94	0.21
2	The white blood cell	LRAC	1300	433.52	0.33
		LRES	500	2223.21	4.45
		SLR	390	141.58	0.36
3	The starfish	LRAC	1500	315.22	0.21
		LRES	275	547.36	1.99
		SLR	310	90.96	0.29
4	The cartoon bear	LRAC	2000	385.07	0.19
		LRES	190	404.92	2.13
		SLR	240	59.92	0.25
5	The CT scan of liver tumor	LRAC	4000	1014.72	0.25
		LRES	620	2514.90	4.06
		SLR	1350	580.55	0.43

An image of two starfish in the third row of **Figure 5** is of size 200×200 pixels. Although the RSF algorithm can separate the two starfish, it shows some noisy pixels within their bodies. As for the LRAC contour in the fourth column, it cannot move into the space in between the two starfish to separate them. The ACWE, LRES, and SLR, on contrary, provide actual boundaries of the two starfish separately. By calculating global means intensity, the ACWE estimates homogeneous textures very well. The scale adaptation process in the LRES and SLR gives advantage in tracing various concave shape. Our SLR consumes only 90.96 seconds for 310 iterations that is quicker than the LRES with 547.36 seconds for 275 iterations.

The fourth row of **Figure 5** is a cartoon image of a bear with size 273×320 pixels. Allowing the user to interact, the initial contour is set manually by clicking points and connecting them to create a closed contour. The ACWE and RSF detect the shadow as the outcome and split the bear into some areas. Small kernel helps the RSF to segment more details than the ACWE. They consume almost similar computing time, i.e., 0.78 and 0.83 second per iteration. While the RSF needs 40 iterations, the ACWE only 10 iterations. With 2000 iterations, the LRAC's contour remains unable to trace concave part between the bear's head and foot. This is because it is difficult to set an optimal scale for object with several concavity. The LRES locates the bear with some miss at the ear part due to the inability of thin search lines to reliably sample the pixels intensity. As a result, the contour front maybe directed in wrong directions. Also, the LRES, requiring 2.13 seconds per iteration, is more time consuming than our SLR, which took only 0.25 second per iteration, yet it can trace the satisfying outcome.

The fifth row of **Figure 5** is a 315 × 368 pixels computed tomography scan of a liver tumor. The global region-based models have a tendency to include more than liver and tumors as the outcome. While the ACWE traces the image with less details, the RSF is able to include the tumors. The LRAC's contour got stucked thus could not grow into the bottom of the liver. The LRES captures the entire liver including half tumor but with spill-over areas on the liver edge. It costs 4.06 seconds for each iteration and 2514.90 seconds in total. Nonetheless, our SLR's contour has enough capture range to reach the liver boundary while excluding some tumor regions. Level set formulation of our SLR allows in handling topological changes of liver and two tumors together. Our SLR is more effective requiring less iteration than the LRAC and

taking less computing time than the LRES, meanwhile, provides more satisfying outcome.

The non-uniform T-shape object in the first row of **Figure 6** is of size 96×127 pixels. The RSF, LRAC, LRES, and SLR are capable of tracking the non-uniform background but the ACWE cannot. The RSF's final contour is properly positioned after 270 iterations consuming 58.48 seconds. The LRAC required 1600 iterations and 213.88 seconds while ignoring intensity details in the T-shape corners. The LRES still considers the shadow as the foreground. Taking only 140 iterations at 17.19 seconds, the T-shape object is captured by our SLR correctly.

The second row of **Figure 6** depicts an image of the left ventricle of a cardiac MRI with size 324×324 where the initial position is put inside the object. Both epicardial and endocardial boundaries are required forming a ring-shape region. The ACWE and RSF classify all bright intensities as the object. While the RSF traces more pixels intensity and handles inhomogeneous background well, the ACWE neglects some pixels intensity and its variation. With $r = 30$, the LRAC contour shranked and disappeared completely. Decreasing r to 25 makes it evolve but stops after 3000 iterations at two intersections. The length between the contour and the object is very distant, increasing the number of iterations to 4000 iterations still does not induce any further evolution. The LRAC's ball lacks of reliable statistics to generate a motion force. As a result, it stuck even with additional 1000 iterations. The LRES's contour confuses and stops at an unintended object. Our presented method capture the concave ring-shape object with enough range with 1700 iterations at 2208.45 seconds.

A heterogeneous texture object without noise in the third row of **Figure 6** is of size 200×200 pixels. The image not only contains both bright and dark intensities on its object and background but also various concave parts. The global mean intensity approximation in ACWE results in image segmentation depending on its intensity where the bright area represents the object and the dark region as the background. The RSF, LRAC, and LRES capture most foreground that can be clearly distinguished. However, they got confused where the object and the background has similar intensity. The total computing times are 160.43, 133.64, and 658.35 seconds. Meanwhile, our scheme obtains a satisfactory result consuming only 68.91 seconds for 350 iterations at the rate 0.19 second per iteration.

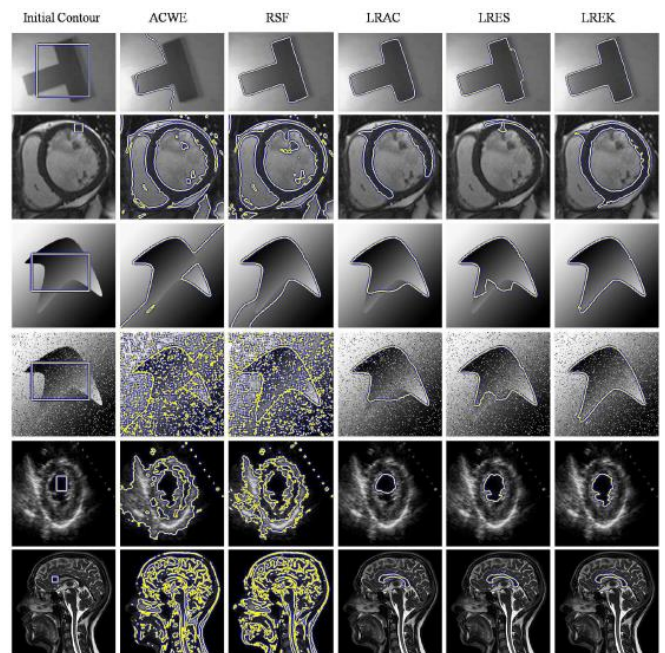


Figure 6. Performance of various active contour scheme; initial and final contour for ACWE, RSF, LRAC, LRES, and SLR, respectively.

Table 2. Computational costs for **Figure 6**.

No.	Image	Method	Number of Iterations	Total Iteration Time (seconds)	Average Time (second per iterations)
1	The T-shape object	LRAC	1600	213.88	0.13
		LRES	100	157.09	1.57
2	The cardiac MRI of left ventricle	SLR	140	17.19	0.12
		LRAC	4000	1071.63	0.26
3	The heterogeneous texture without noise	SLR	1700	2208.45	2.94
		LRAC	550	724.93	0.42
4	The heterogeneous textures with salt and pepper noise	LRES	300	133.64	0.24
		SLR	350	658.35	2.19
5	The ultrasound image of left ventricle	LRAC	550	68.91	0.19
		LRES	300	280.65	0.51
6	The corpus callosum	SLR	400	305.06	0.28
		LRAC	300	923.96	0.66
		LRES	240	29.99	0.12
		SLR	150	98.49	0.63

The fourth row of **Figure 6** depicts the same object as in the third row with additional salt and pepper noise. The ACWE needs 10 iterations with 21.48 seconds to partition the image according to bright and dark intensity and also capturing the white and black noise. The RSF requires 30 iterations to produce most of the object and the noise as the outcome. This is an effect of convolving local window over the entire image. It is different from the LRAC, LRES and SLR that employ the local image feature and computed it within local windows only on the contour. However, the LRAC and LRES could not trace correctly the bottom area that is hardly distinguishable from the background. Our method in the last column provides a complete result in the presence of noise with the speed of 0.28 second per iteration.

An ultrasound image of left ventricle of size 221×217 is shown in the fifth row of **Figure 6**. The ACWE and RSF consider all bright parts as the foreground. the RSF is able in segmenting non-uniform intensity whereas the ACWE is unable. The SLR behaves in similar manner as the LRAC and LRES. Although the number of iterations is set to 300, the diminished capture range still exists and it prevents the contour to further evolve into the bottom part. The LRES that uses adaptive search line does not suffer from such problem. However, it still has problem segmenting the bottom part due to the intensity is the same with the background. The expandable kernel of SLR contributes to a more satisfying result although its initial size is defined as 15 pixels equal to that of the LRAC scheme.

An MRI image of a corpus callosum of the brain in the sixth row of **Figure 6** is of size 550×550 where its initial contour is positioned to the right of the corpus callosum. The ACWE and RSF have a tendency to capture the entire image instead of just the corpus callosum. The LRAC, LRES and SLR contours are capable of tracing the deep concave object. By setting the LRAC's ball radius and SLR's kernel size as 15 pixels, the LRAC's contour is stucked. Its scale is then adjusted to 20 pixels to capture with a larger range. The local adaptation process provides the enough capture range to capture a corpus callosum entirely using 15 pixels. Moreover, it needs 1000 iterations less than the 2500 iterations required by the LRAC. It converges to the final result faster consuming only 305.06 seconds which is a lot less than the LRES at 923.96 seconds.

The X-ray hand image in **Figure 7** has size 255×180 pixels. The first row of **Figure 7** depicts the performance in segmenting just the bone part. The ACWE and RSF

almost capture the entire bone but the ACWE traces more skin area than the RSF. The LRAC's contour could not propagate into the concave fingers and the bottom hand caused by a small capture range. The LRES could arrive only into the concave areas of the fingers. The information on the search line could not generate enough force to segment the bottom part of the hand. Meanwhile, our method captures the fingers with a larger range and the bottom area of the hand segmenting entire bone and excluding the skin area entirely. Also, we notice that the SLR's contour splits excluding skin pixels on the bottom part.

The second row of **Figure 7** shows segmentation of the hand including skin region instead of just the bone. Although the sizes of the RSF's Gaussian function and of the LRAC's window are set with a large value, they produce similar segmentation results with the ACWE. In our formulation, the Gaussian function is used to capture any blur or smooth edge.

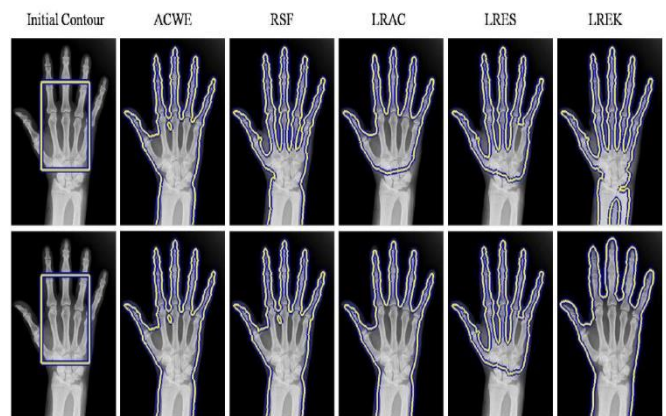


Figure 7. Performance of several active contour models for bone part an X-ray hand image in the upper row and skin part in the lower row [32].

The Gaussian SLR with large sigma provides almost all the skin area. the RSF cannot trace the smooth boundary using both small and large scales Gaussian kernel. The RSF produces accurate segmentation using small sigma. With extremely large sigma, it fails to capture some small details.

The Directional Scalable Local Regional (DSLR) Feature

This subsection shows the performance of our directional SLR (DSLR) on real medical images. The initial and final contours of the positive-edge and negative-edge objects are put on the original images in the first, second, and third row of **Figure 8**, respectively. Each

tested image contains several objects with different kind of the edge. They are the object with positive edge defined as a dark foreground lying on a bright background and the object with negative edge as a bright foreground on a dark background.

The first column of **Figure 8** contains two objects of interest, i.e., a lateral ventricle as the object with positive edge and a bright spot of a tumor as the object with negative edge. Our DSLR's contour accurately stops at the two desirable boundaries using one initial contour. By setting $\beta = +1$, the lateral ventricle can be correctly positioned. β is set to -1 to achieve the boundary of the bright spot of the tumor.

The second column of **Figure 8** depicts segmentation results of an ultrasound image. In the second row, we intend to capture the womb and the baby, considered as the positive-edged and negative-edged objects, respectively. The negative value of ω helps to direct the contour to meet the womb. When the contour is close to the desired object, the force turns into the SLR force. Otherwise, the contour would continue to grow outwards ignoring the womb boundary. In the third row, we set $\beta = -1$ and $\omega = +1$ to give an inward direction of the contour front to capture the small baby, our desired negative-edged object.

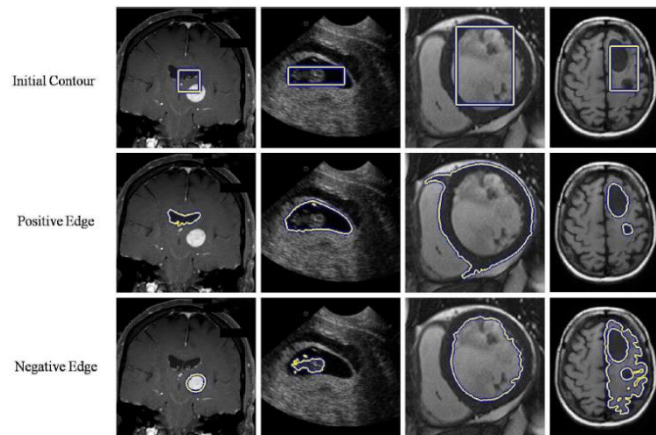


Figure 8. Performance of our DSLR for various medical images [37].

In the third column of **Figure 8**, the image of MRI left ventricle has two targeted objects. By setting β to $+1$, the positive-edged epicardial boundary is traced as depicted in the second row. On the other hand, negative-edged endocardium can be segmented by letting β be -1 . The value of ω is selected to be -1 so that the local motion constant navigates outward to

trace the epicardial part and $\omega = +1$ is selected to propagate the contour inward to detect the endocardium as shown in the third row. The force turns into the SLR force after it covers the intended edge's type pixels.

In the fourth column of **Figure 8**, the two dark spots of the tumors are considered as two separated positive-edge objects. They are our segmentation goal shown in the second row. The right part of the brain with two separated lumps of tumor inside is considered as the negative-edged object. With the benefit of level set implementation, our DSLR contour splits by itself and captures the two separated tumors properly. Also, the right part of the brain, our desired negative-edged object, can be traced accurately without any leaks into the tumors or the left part as shown in the third row.

Conclusions

An active contour method that utilizes scalable local regional (SLR) statistics on expandable kernels has been presented. The performance of our SLR active contour are compared with the other active contour schemes. Our scheme is less sensitive to noise than the other global models (the ACWE and the RSF). Although the RSF model used the Gaussian kernel, there is no significant difference using small or large Gaussian sigma. Our SLR with Gaussian function is capable in capturing the blur boundary. The superiority of our active contour over the LRAC is the ability to capture the concave boundary with a large range. When compared to the LRES, our method produces more efficient outcomes. The LRES's search line could not sample the pixel intensity well, thus, the contour may get confused and unable to move to the true boundary. Moreover, the unscalability characteristics of the line leads to expensive computation. On the other hand, the scalability of the kernel helps to maintain its scale proportional to the change of image size which leads to rapid convergence.

The experiments have verified that our SLR produces more satisfying and efficient segmentation results. Local region-based statistics makes our model robust in tackling noisy environment and inhomogeneous background. The expandable kernel enables in capturing the boundary concavity with a large range. Our SLR with Gaussian function is capable to detect the blur boundary. The experiments validate that our additional directional edge's type selectivity feature is capable to extract different kind of the edges conveniently using

Original Article

the same initial position. The scalable kernel samples intensity statistics appropriately deemphasizing the presence of noise by taking local intensity averages. The level set implementation allows the contour to split and merge when needed.

Conflicts of interest

There are no conflicts to declare.

Acknowledgements

This work was funded by AUN/SEED-Net JICA.

References

- [1] M. Kass, A. Witkin, and D. Terzopoulos, Snakes: Active contour models, *Int. J. Comput. Vis.*, vol. 1, no. 4, pp. 321-331, Jan. 1988.
- [2] C. Zimmer and J.-C. Olivo-Marin, Coupled parametric active contours, *IEEE Trans. Pattern Anal. Mach. Intell.*, vol. 27, no. 11, pp. 1838-1842, Nov. 2005.
- [3] V. Caselles, R. Kimmel, and G. Sapiro, Geodesic active contours, *Int. J. Comput. Vis.*, vol. 22, no. 1, pp. 61-79, 1997.
- [4] C. Xu and J. L. Prince, Snakes, shapes, and gradient vector flow, *IEEE Trans. Image Process.*, vol. 7, no. 3, pp. 359-369, Mar. 1998.
- [5] B. Li and S. T. Acton, Active contour external force using vector field convolution for image segmentation, *IEEE Trans. Image Process.*, vol. 16, no. 8, pp. 2096-2106, Aug. 2007.
- [6] T. Wang, I. Cheng, and A. Basu, Fluid vector flow and applications in brain tumor segmentation, *IEEE Trans. Biomed. Eng.*, vol. 56, no. 3, pp. 781-789, Mar. 2009.
- [7] S. Osher and J. Sethian, Front propagating with curvature-dependent speed: Algorithms based on Hamilton-Jacobi formulations, *J. Comput. Phys.*, vol. 79, no. 1, pp. 12-49, Nov. 1988.
- [8] H.-K. Zhao, T. F. Chan, B. Merriman, and S. Osher, A variational level set approach to multiphase motion, *Journal of Computational Physics*, vol. 127, pp. 179-195, 1996.
- [9] D. Mumford and J. Shah, Optimal approximation by piecewise smooth functions and associated variational problems, *Commun. Pure Appl. Math.*, vol. 42, pp. 577-685, 1989.
- [10] A. Tsai, A. Yezzi, and A. S. Willsky, Curve evolution implementation of the Mumford-Shah functional for image segmentation, denoising, interpolation, and magnification, *IEEE Trans. Image Process.*, vol. 10, no. 8, pp. 1169-1186, Aug. 2001.
- [11] L. A. Vese and T. F. Chan, A multiphase level set framework for image segmentation using the Mumford and Shah model, *Int. J. Comput. Vis.*, vol. 50, no. 2, pp. 271-293, Dec. 2002.
- [12] T. F. Chan and L. A. Vese, Active contours without edges, *IEEE Trans. Image Process.*, vol. 10, no. 2, pp. 266-277, Feb. 2001.
- [13] J. A. Yezzi, A. Tsai, and A. Willsky, A fully global approach to image segmentation via coupled curve evolution equations, *J. Vis. Commun. Image Represent.*, vol. 13, no. 1, pp. 195-216, Mar. 2002.
- [14] O. Michailovich, Y. Rathi, and A. Tannenbaum, Image segmentation using active contours driven by the Bhattacharyya gradient flow, *IEEE Trans. Image Process.*, vol. 16, no. 11, pp. 2787-2801, Nov. 2007.
- [15] A. Bhattacharyya, On a measure of divergence between two statistical populations defined by their probability distributions, *Bull. Calcutta Math. Soc.*, vol. 35, pp. 99-109, 1943.
- [16] C. Li, C. Kao, J. C. Gore, and Z. Ding, Minimization of region-scalable fitting energy for image segmentation, *IEEE Trans. Image Process.*, vol. 17, no. 10, pp. 1940-1949, Oct. 2008.
- [17] K. W. Sum and P. Y. S. Cheung, Vessel extraction under non-uniform illumination: A level set approach, *IEEE Trans. Biomed. Eng.*, vol. 55, no. 1, pp. 358-360, Jan. 2008.
- [18] M. Jung, G. Peyr and L. D. Cohen, Nonlocal active contour, *SIAM J. Imag. Sci.*, vol. 5, no. 3, pp. 1022-1054, 2012.
- [19] T. Brox and D. Cremers, On local region models and a statistical interpretation of the piecewise smooth Mumford-Shah functional, *Int. J. Comput. Vis.*, vol. 84, pp. 184-193, 2008.
- [20] J. Piovano, M. Rousson, and T. Papadopoulo, Efficient segmentation of piecewise smooth images, in F. Sgallari, A. Murli, and N. Paragios (Eds.) *Scale space and variational methods in computer vision (SSVM)*, LNCS: Vol. 4485, pp. 709-720. Springer, Heidelberg, 2007.
- [21] C. Li, R. Huang, Z. Ding, C. Gatenby, D. N. Metaxas, and J. C. Gore, A level set method for image segmentation

Journal of Science and Applicative Technology

- in the presence of intensity inhomogeneities with application to mri, *IEEE Trans. Image Process.*, vol. 20, pp. 2007-2016, Jul. 2011.
- [22] H. Zhang, X. Ye, and Y. Chen, An efficient algorithm for multiphase image segmentation with intensity bias correction, *IEEE Trans. Image Process.* vol. 22, no. 10, pp. 3842-3851, May 2013.
- [23] J. Piovano and T. Papadopoulo, Local statistics based region segmentation with automatic scale selection, in the *Eur. Conf. Computer Vision (ECCV)*, vol. 5303, pp. 486-499, Marseille, 2008.
- [24] S. Lankton and A. Tannenbaum, Localizing region-based active contours, *IEEE Trans. Image Process.*, vol. 17, no. 11, pp. 2029-2039, Nov. 2008.
- [25] C. Darolli, A. Mertins, C. Bodensteiner, and U. G. Hofmann, Local region descriptors for active contours evolution, *IEEE Trans. Image Process.*, vol. 17, No. 12, pp. 2275-2288, Dec. 2008.
- [26] P. Karaolani, G. D. Sullivan, and K. D. Baker, Active contours using finite element to control local scale, Proceeding of British Machine Vision Conference (BMVC), pp. 481-487, 1992.
- [27] S. Phumeechanya, C. Pluempiwiriyawej, and S. Thongvigitmanee, Active contour using local regional information on extendable search lines (LRES) for image segmentation, *IEICE Trans. Inf. Syst.*, vol. E93-D, no. 6, pp. 1625-1635, Jun. 2010.
- [28] T. F. Cootes, C. J. Taylor, D. H. Cooper, and J. Graham, Active shape models - their training and application, *Comput. Vis. Image Underst.*, vol. 56, no. 3, pp. 35-59, Jan. 1995.
- [29] J. Mille, Narrow band region-based active contours and surfaces for 2D and 3D segmentation, *Comput. Vis. Image Underst.*, vol. 113, no. 9, pp. 946-965, Sep. 2009.
- [30] H. Li and A. Yezzi, Local or global minima: flexible dual-front active contours, *IEEE Trans. Pattern Anal. Mach. Intell.*, vol. 29, no. 1, pp. 1-13, Jan. 2007.
- [31] R. Ronfard, Region-based strategies for active contour models, *Int. J. Comput. Vis.*, vol. 3, no. 2, pp. 229-251, 1994.
- [32] A. Faisal and C. Pluempiwiriyawej, Active contour using local region-scalable force with expandable kernel, Proc. 2012 IEEE Int. Conf. Information Science and Technology (ICIST), pp. 18-24, Wuhan, China, Mar. 23-25, 2012.
- [33] H. Park, T. Schoepflin, and Y. Kim, Active contour model with gradient direction information: directional snake, *IEEE Trans. Image Process.*, vol. 11, no. 2, pp. 252-256, Feb. 2001.
- [34] J. Tang, S. Millington, S. T. Acton, J. Crandall, and S. Hurwitz, Surface extraction and thickness measurement of the articular cartilage from MR images using directional gradient vector flow snakes, *IEEE Trans. Biomed. Eng.*, vol. 53, no. 5, pp. 896-907, May. 2006.
- [35] J. Cheng and S. W. Foo, Dynamic directional gradient vector flow for snakes, *IEEE Trans. Image Process.*, vol. 15, no. 6, pp. 1563-1571, Jun. 2006.
- [36] S. Phumeechanya, C. Pluempiwiriyawej, and S. Thongvigitmanee, Edge's type selectable active contour using local regional information on extendable search line, Proc. of 2010 IEEE Int. Conf. Image Processing (ICIP), pp. 653-656, Hong Kong, Sep. 26-29, 2010.
- [37] A. Faisal and C. Pluempiwiriyawej, Directional local region-scalable active contour with expandable kernel, Proc. of 2012 Int. Conf. Electrical Engineering/Electronics, Computer, Telecommunication, and Information Technology (ECTI-CON), Hua Hin, Thailand, May 16-18, 2012.
- [38] K. Zhang and L. Zhang and K. M. Lam and D. Zhang, A Level Set Approach to Image Segmentation With Intensity Inhomogeneity, *IEEE Trans. Cybern.*, vol. 46, no. 2, pp. 546-557, Feb 2016.
- [39] S. Mukherjee and S. T. Acton, Region Based Segmentation in Presence of Intensity Inhomogeneity Using Legendre Polynomials, *IEEE Signal Process. Lett.*, vol. 22, no. 3, pp. 298-302, Mar 2015.
- [40] C. Li, R. Huang, Z. Ding, C. Gatenby, D. N. Metaxas and J. C. Gore, A level set method for image segmentation in the presence of intensity inhomogeneities with application to MRI, *IEEE Trans. Image Process.*, vol. 20, no. 7, pp. 2007-2016, Jul 2011.
- [41] Xiao-Feng Wang, Hai Min, Le Zou and Yi-Gang Zhang, A novel level set method for image segmentation by incorporating local statistical analysis and global similarity measurement, *Pattern Recogn.*, vol. 48, no. 1, pp. 189-204, Jan 2015.
- [42] K. Zhang AND L. Zhang AND H. Song AND D. Zhang, Reinitialization-free level set evolution via reaction

- diffusion, *IEEE Trans. Image Process.*, vol. 22, no. 1, pp. 258-271, Jan 2013.
- [43] C. Li AND C. Xu AND C. Gui AND M. D. Fox, Distance regularized level set evolution and its application to image segmentation, *IEEE Trans. Image Process.*, vol. 19, no. 12, pp. 3243-3254, Dec 2010.
- [44] A. Faisal, S. C. Ng, and K. W. Lai, Multiple active contours using scalable local regional information on expandable kernel, Proc. of 2014 IEEE Conference on Biomedical Engineering and Sciences (IECBES), Miri, Sarawak, Malaysia, 8 - 10 December 2014.
- [45] A. Faisal, S. C. Ng, and K. W. Lai, Multiple LREK active contours for knee meniscus ultrasound image segmentation, *IEEE Trans. Med. Imag.*, vol. 34, no. 10, pp. 2162-2171, Oct 2015.